THE EFFECTIVENESS OF PUBLISHED CONTINUUM CONSTITUTIVE LAWS TO PREDICT STRESS ASSISTED DENSIFICATION OF POWDER COMPACTS

I. M. Espinoza-Ochoa[1], H. Camacho-Montes[1,*], Y. Espinosa-Almeyda[1], C. A. Rodríguez-González[1], R. K. Bordia[2]

[1]Instituto de Ingeniería y Tecnología, Universidad Autónoma de Ciudad Juárez, Av. Del Charro 450 Norte, Cd. Juárez, Chihuahua 32310, México.
[2]Department of Materials Science and Engineering, Clemson University, 161 Sirrine Hall, Clemson, SC 29634, USA.

Corresponding author: H. Camacho-Montes (hcamacho@uacj.mx)

Abstract

Commonly used constitutive laws for crystalline and viscous materials have been compared to predict the densification behavior under hot-pressing and sinter-forging. Experimental results, from literature for one loading condition, have been used to extract the constitutive laws for amorphous and crystalline materials and, these in-turn, have been used to predict behavior under a different set of loading conditions. Ideally, the constitutive parameters obtained from one set of loading conditions and thermal history should apply to a different set of conditions. However, there is a lack of systematic experimental studies in which this can be checked. In this paper, we use constitutive parameters obtained from one set of conditions to predict the densification response under a different set of loading conditions. For both sintering of amorphous and crystalline materials, we use two different constitutive parameters and compare the predictions of these for the case where experimental results are not available. In addition, the effect of temperature on densification behavior for stress-assisted sintering has been investigated. It is shown that the two commonly used constitutive models for viscous sintering (Scherer and Skorohod–Olevsky) predict similar behavior for amorphous materials. However, for crystalline materials, the predictions of the Riedel–Svoboda (RS) and the Kuhn–Sofronis–McMeeking (KSM) models are different. Finally, it is shown that the dependence of the normalized densification on temperature, under

constant heating rate conditions, with parameters obtained from isothermal experiments, is a good test for the models.

Keywords: Stress-assisted densification, power-law creep model

1. INTRODUCTION

Thermo-mechanical processes are commonly used to consolidate ceramic powders. Hot-pressing and hot-forging are two examples of significant application and intensive research [1,2]. An external pressure increases the sintering driving force leading to faster densification. Thus, pressure-assisted sintering is a means to densify materials which are normally resistant to sintering. Because of the enhanced densification, and by implication improved performance, sintering with an external pressure has been used in demanding applications in aerospace, biomedical, and electronic applications where high density is a requirement [3].

Hot-pressing and sinter-forging have been reported on a variety of structural and electronic ceramics [4-11]. For example, hot-pressing has been used in the development of composites with significantly higher thermal conductivities and in the densification of ultrahigh temperature ceramics [12-15]. Guillon [16] carefully studied the effect of applied stress on field assisted sintering. Stress assisted grain growth has also been a topic of interest [17,18]. Modeling efforts for a better understanding and control of these processes has also received significant attention [19-26]. For example, Wakai et al. [27] modeled the elimination of strength-limiting defects by pressure assisted sintering at low stress levels.

Simulation has proved to be a useful tool to characterize powder densification. For example, Bragnisky et al. [28] developed numerical model capable of simulating microstructural evolution and macroscopic deformation during sintering of complex powder compacts. Van Nguyen et al. [29] developed a model for powder metal hot-isostatic-pressing (PM-HIP) where the contribution of several mechanisms to densification is analyzed. Theoretical and numerical models have been developed for microwave-assisted sintering [30] and spark-plasma sintering [31]. Yin et al. [32] describe the effect of molding pressure on densification of microwave-sintered ceramic tool material by simulations and experiments. Bouvard et al. [33-35] have reported the use of micromechanical

modeling, as well as phenomenological and power law creep approaches, to develop constitutive laws for powder compacts.

The densification during stress assisted sintering of ceramics is attributed to a combination of pore-curvature-driven diffusion [36-38], stress-driven diffusion [4], and/or plastic flow [39]. The intrinsic driving force for densification is often represented by the so-called sintering pressure [40,41]. The application of an external pressure acts as an additional driving force for densification [42], which can be used to further reduce sintering time and temperature. The sensitivity of the densification to applied uniaxial stress for hot-pressing and sinter-forging has been reported by Camacho-Montes et al. [43].

Reiterer and Ewsuk [44] have reviewed and compared four widely used approaches to study sintering: i) The Riedel and Svoboda model (RS) for solid state sintering [45,46]; ii) Skorohod and Olevsky viscous sintering (SOVS) model for viscous sintering [47]; iii) Kinetic Monte Carlo model (KMC) [28,48,49]; and iv) the master sintering curve approach (MSC) [50,52]. Each one has its own strengths and weaknesses. As shown in Ref. [44], the KMC model provides a description for structural evolution. The RS, SOVS, and KMC models are good approaches for the prediction of the densification response. However, the RS model is more difficult to use than the other ones; the SOVS model cannot predict microstructural evolution; and the KMC and MSC models do not consider stress in their mathematical description making them unsuitable for stress assisted sintering.

In a comprehensive review of sintering, Bordia, Kang, and Olevsky analyzed the status and the challenge of sintering science and technology [53]. The continuum mechanics formulation [40,47,54] of sintering is reported as the tool to investigate the macroscopic factors involved in the response of a sintering body to a general stress state. For the investigation of sintering under either external or internal stresses, a basic continuum mechanics approach has been developed in Refs. [40,41,47]. An essential element of this approach is the constitutive laws which govern the material response to both constrained and stress-assisted sintering. In the literature, several constitutive laws have been proposed and used for specific systems or cases. However, further critical evaluation for the same problem or the same material system, using different proposed constitutive laws is needed to determine the broader applicability of the constitutive laws.

In the present work, comparison of four constitutive models is presented. The power-law creep model developed by Kuhn and McMeeking [22] and Sofronis and McMeeking [23] are considered. The

implementation proposed here for the Khun-Sofronis-McMeeking model is similar to that reported by Bhattacharya et al. [21]. The Riedel-Svoboda model [45,46,55] for diffusion-controlled deformation for polycrystalline materials is also considered. These two constitutive laws are appropriate for crystalline materials. For the constitutive relations of viscous materials, the Scherer cell model [56] and the Skorohod-Olevsky model [47] are applied. Published experimental results, under one set of loading conditions, are used to extract the constitutive parameters for both amorphous and crystalline materials and these are applied to predict the densification behavior under a different set of loading conditions. In addition, the effect of temperature on the sensitivity of constitutive parameters is explored during stress assisted sintering.

2. PROBLEM SETUP

The prediction of densification and stress distribution during the sintering process is performed using four constitutive behaviors that are implemented into the user defined subroutine CREEP of ABAQUS, using a similar algorithm to that proposed by Bhattacharya et al. [21]. Because of the axisymmetry along the z-axis, an axisymmetric finite element model is developed for the cylindrical sample. A bilinear axisymmetric element (C0AX4) is chosen. The friction between the die walls and the compact has been neglected. Figure 1 is a schematic of the problem setup.

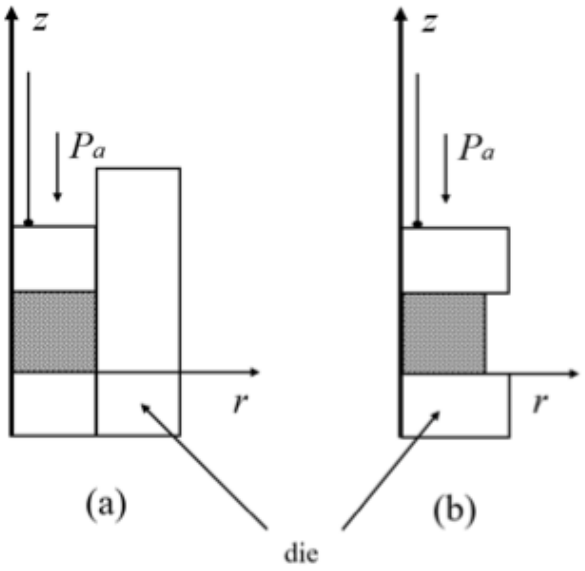

Fig. 1. (a) *Hot-pressing situation for case I and* (b) *sinter-forging situation for case II* (*uniaxial stress applied through the piston*).

For the numerical experiments, two macroscopic cases, labeled as case I or hot-pressing (Fig. 1(a)) and case II or sinter-forging (Fig 1 (b)), are performed. For case I, the powder compact is confined inside a die under uniaxial stress, P_a, applied by the piston (Fig. 1(a)). For case II, the powder compact is not confined in the radial direction perpendicular to the direction in which the stress is applied (Fig. 1(b)).

Fundamentally, the sintering simulation consists of two steps: A general static step followed by a viscous step. The load and the boundary conditions are applied in the general static step. The elastic stress distribution within the powder compact is calculated by ABAQUS, followed by transferring the stress tensor into the viscous analysis. In this step, the CREEP subroutine is called to calculate the creep strain and update the dimensions and the relative density. The newly computed values are returned to ABAQUS, where the stress tensor is redetermined. Material properties in ABAQUS need to be updated with the evolution of the density. This function is performed by the USDFLD subroutine [57]. This sequence is repeated for each time step. The flow chart of the simulation is presented in Fig. 2.

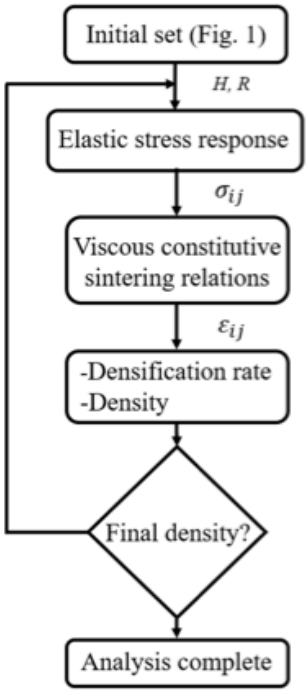

Fig. 2. *Schematic flow chart for the computation of density evolution. H is the powder compact height, R is its radius, σ_{ij} is the stress tensor and ε_{ij} is the strain tensor*

The user defined CREEP subroutine is based on the following equation:

$$\dot{\varepsilon}_{ij} = \frac{3\left(\sigma_{ij} \pm \delta_{ij}\sigma_m\right)}{2q}\Delta\dot{\varepsilon}_{cr} + \frac{I_{ij}}{3}\Delta\dot{\varepsilon}_{sw}, \quad (1)$$

where $\dot{\varepsilon}_{ij}$, $\dot{\varepsilon}_{cr}$, and $\dot{\varepsilon}_{sw}$ are the strain rate tensor, the creep rate, and the volumetric strain rate, respectively. The increments $\Delta\dot{\varepsilon}_{cr}$, and $\Delta\dot{\varepsilon}_{sw}$ are functions of the von Mises stress q, and the hydrostatic stress σ_m, respectively. The mathematical symbol $\pm$ in front of term $\delta_{ij}\sigma_m$ represents a generalization and it adapts to each specific model as shown below. The functions can be implemented in the ABAQUS user subroutine. Solution-dependent state variables can also be employed. For the herein considered constitutive behaviors, density is taken as a state variable. For the non-isothermal cases, the temperature is found as a function of time, and the temperature–dependent properties can be obtained. I_{ij} is the identity matrix because swelling components are considered isotropic [58]. Finally, $\Delta\dot{\varepsilon}_{cr}$, and $\Delta\dot{\varepsilon}_{sw}$ are defined for each one of the constitutive behaviors and they are calculated for each ABAQUS CREEP personalized subroutine [58].

Four constitutive behaviors have been considered: The Scherer (identified as the S) model [56] and the SOVS model [47] are used to describe the linear viscous behavior of amorphous ceramics. For polycrystalline ceramics, the non-linear extension [55] of the Riedel-Svoboda (RS) model [19,46] and the power law creep behavior described by a combination of Kuhn-McMeeking [22] and Sofronis-McMeeking [23] (KSM) have been used. The combinations of Case I (hot-pressing) and II (sinter-forging) with the four previously mentioned constitutive behaviors lead to the eight numerical experiments shown in Table 1.

Table 1. *Four different constitutive behaviors identified in the first column are considered for cases I and II resulting in eight numerical experiments*.

Cases	Case I (see Fig. 1(a))	Case II (see Fig. 1(b))
Kuhn–Sofronis–McMeeking (KSM)	KSM-I	KSM-II
Riedel-Svoboda (RS)	RS-I	RS-II
Scherer (S)	S-I	S-II
Skorohod – Olevsky (SOVS)	SOVS-I	SOVS-II

2.1 *Elastic stress equilibrium*

The continuum equilibrium equation is defined by

$$\sigma_{ij,j} = 0, \tag{2}$$

where σ_{ij} is the stress tensor of second order and the comma notation indicates the partial derivate relative to the x_j component at the Cartesian coordinate system $\mathbf{x} = (x_1, x_2, x_3)$; i.e., $f_{i,j} = \partial f_i / \partial x_j$.

The strain tensor of second order, ε_{ij}, is given in terms of displacements, u_i, as

$$\varepsilon_{ij} = \left(u_{i,j} + u_{j,i}\right)/2, \tag{3}$$

and the Hooke law is taken as the constitutive relation where the dependence of elastic modulus (E_{0p}) and elastic Poisson's ratio (ν_{0p}) on porosity, *f*, have the form [59]:

$$E_{0p} = E_0\left(1 - \frac{f}{0.652}\right)^{2.23}, \tag{4}$$

$$\nu_{0p} = 0.14 + \left(1 - \frac{f}{0.5}\right)^{1.22}\left(\nu_s - 0.14\right), \tag{5}$$

where E_0 and ν_s are the elastic modulus and Poisson ratio for a fully dense body.

The boundary conditions may be stated as:

$$\sigma_{ij}\big|_{BS} = \phi_1, \tag{6}$$

$$u_i\big|_{BS} = \phi_2, \tag{7}$$

where *BS* denotes the boundary surface for the powder compact. The Eqs. (2)-(7) define a mathematical stress equilibrium problem that has a unique solution if the boundary conditions, Eqs. (6) and (7), are properly stated. The calculations are implemented through the software ABAQUS CAE/16.14. The expressions ϕ_1 and ϕ_2 take their values depending on the loading case, as shown in Table 2.

Table 2. *Boundary conditions for the hot-pressing experiments (I) and the sinter-forging experiments (II) associate to the stress equilibrium problem.*

	Hot-pressing experiments I	Sinter-forging experiments II
$\phi_1(z=H)$	$\delta_{ij}P_a$	$\delta_{ij}P_a$
$\phi_2(r=R, z=0)$	$u_r=0,\ u_z=0,$	free, $u_z=0$

2.2 *The Scherer Model*

The stress distribution calculated in the elastic problem (Eqs. (2)-(7)) is imported in a viscous problem defined by the constitutive equations presented, for instance in Ref. [40,41]:

$$\dot{\varepsilon}_x = \dot{\varepsilon}_f + E_p^{-1}\left[\sigma_x - \nu_p\left(\sigma_y + \sigma_z\right)\right], \tag{8}$$

$$\dot{\varepsilon}_y = \dot{\varepsilon}_f + E_p^{-1}\left[\sigma_y - \nu_p\left(\sigma_x + \sigma_z\right)\right], \tag{9}$$

$$\dot{\varepsilon}_z = \dot{\varepsilon}_f + E_p^{-1}\left[\sigma_z - \nu_p\left(\sigma_x + \sigma_y\right)\right], \tag{10}$$

where E_p, ν_p and $\dot{\varepsilon}_f$ are the uniaxial viscosity, the viscous Poisson coefficient, and the free sintering strain rate, respectively of the porous body. Re-writing Eqs. (8)-(10) in compact form, we have:

$$\dot{\varepsilon}_{ij} = \frac{q}{2G_p}\left(\frac{\sigma'_{ij}}{q}\right) + \frac{1}{3}\frac{\sigma_m - \sigma_{s(S)}}{K_p}\delta_{ij}, \tag{11}$$

where, G_p and K_p are the shear and bulk viscosity respectively. σ'_{ij} is the deviatoric stress.

By comparing the first and second terms of Eq. (1) with those of Eq. (11), the following strain increments can be obtained:

$$\Delta\dot{\varepsilon}_{cr} = q/\left(3G_p\right), \tag{12}$$

$$\Delta\dot{\varepsilon}_{sw} = \left(\sigma_m - \sigma_s\right)/K_p, \tag{13}$$

where q is the Von Mises equivalent stress, σ_m is the mean or hydrostatic stress calculated in the elastic step, $\sigma_{s(S)}$ is the sintering stress for the Scherer model, and δ_{ij} is the Kronecker delta. In addition, K_p and G_p can be computed by:

$$G_p = E_p \big/ \left(2 + 2\nu_p\right), \tag{14}$$

$$K_p = E_p \big/ \left(3 - 6\nu_p\right). \tag{15}$$

The uniaxial viscosity E_p and the viscous Poisson ratio ν_p for the Scherer model can be found in Ref. [56]. The sintering stress, $\sigma_{s(S)}$, is related to the free sintering rate through the bulk viscosity as reported in Ref. [40]:

$$\sigma_{s(S)} = 3K\dot{\varepsilon}_f. \tag{16}$$

The free sintering rate, $\dot{\varepsilon}_f$, can be calculated using the equations reported by Scherer [56] or the one reported by Mackenzie-Shuttleworth [60]:

$$\dot{\varepsilon}_f = -\frac{1}{2}\left(\frac{4\pi}{3}\right)^{1/3}\left(\frac{\gamma n^{1/3}}{\eta}\right)\left(\frac{1}{\rho}-1\right)^{2/3}, \tag{17}$$

where ρ is the relative density, γ the surface energy, n the number of particles per unit volume, and η the uniaxial viscosity for the fully dense material .

The effect of temperature is through the temperature dependence of viscosity η, that is,

$$\eta = \eta_0 \exp\left(\frac{Q}{RT}\right), \tag{18}$$

where Q is the activation energy, RT is the molar gas constant times the absolute temperature, and η_0 is the pre-exponential factor for viscosity. Furthermore, the densification rate $\dot{\rho}$ is calculated as follows:

$$\dot{\rho} = -\rho\dot{\varepsilon}_{kk}, \tag{19}$$

where $\dot{\varepsilon}_{kk}$ is the trace or the hydrostatic strain rate of the sample (repeated indices imply summation).

2.3 *The Skorohod-Olevsky viscous sintering model*

For the Skorohod-Olevsky (SOVS) model [47], the macroscopic strain tensor is calculated by:

$$\dot{\varepsilon}_{ij} = \frac{\sigma'_{ij}}{2G_{\mathrm{SOVS}}} + \frac{\left(\sigma_m - \sigma_{s(\mathrm{SOVS})}\right)}{3K_{\mathrm{SOVS}}}\delta_{ij}, \tag{20}$$

where $\sigma_{s(\mathrm{SOVS})}$ is the sintering stress for the SOVS model. G_{SOVS} and K_{SOVS} represent the effective shear and bulk viscosities for the SOVS model, which depends on the normalized viscosities ψ (bulk) and φ (shear), and on the material viscosity η whose temperature dependence is given by Eq. (18). After calculating the strain rate components from Eq. (18), they are written in terms of $\Delta\varepsilon^{cr}$ and $\Delta\varepsilon^{sw}$ using Eq. (1) which in turn are related to the bulk and shear viscosity as given in Eqs. (12) and (13). The density increment is given by Eq. (19).

The effective shear and bulk viscosity are defined as:

$$G_{\mathrm{SOVS}} = \eta\psi, \tag{21}$$

$$K_{\mathrm{SOVS}} = 2\eta\psi. \tag{22}$$

Here, the bulk normalized viscosity ψ and the sintering stress $\sigma_{s(\mathrm{SOVS})}$ can be computed as follows

$$\psi = a_2\rho^{b_2}/\left(1-\rho\right)^{c_2}, \tag{23}$$

$$\sigma_{s(\mathrm{SOVS})} = 3a_3\rho^{b_3}\gamma/r, \tag{24}$$

where a_2, b_2, c_2, a_3, and b_3 are adjustable parameters. Also, in Eq. (24), the symbols γ and r represent the surface energy and the grain radius, respectively.

Finally, the density increment is given by Eq. (19) as a function of the strain rate (Eq. (20)).

2.4 *The Riedel-Svoboda Model*

For the Riedel-Svoboda Model, the constitutive equation is defined as follows:

$$\dot{\varepsilon}_{ij} = \frac{\sigma'_{ij}}{2G_{RS}} + \frac{\sigma_m - \sigma_{s(RS)} + \Delta p_{RS}}{3K_{RS}}\delta_{ij}, \tag{25}$$

where Δp_{RS} is the gas overpressure which may develop in closed pores. $\sigma_{s(RS)}$ is the sintering stress for the RS model. K_{RS} and G_{RS} represent the bulk and shear viscosities, which are related to the linear viscosities K_{lin} and G_{lin}, see for instance Refs. [55], through the following relations:

$$K_{RS} = K_{lin}\left(1+\frac{\alpha}{\bar{\sigma}r^2}\right), \tag{26}$$

$$G_{RS} = G_{lin}\left(1+\frac{\alpha}{\bar{\sigma}r^2}\right), \tag{27}$$

where α is a free parameter which determine the deviation from linearity, r is the grain radius size, and $\bar{\sigma}$ is the effective stress defined by the expression

$$\bar{\sigma} = \frac{1}{2}\left|\sigma_m - \sigma_{s(RS)} + \Delta p_{RS}\right| + \frac{1}{2}q\,. \tag{28}$$

In addition, for crystalline materials, both effective viscosity and the sintering stress depend on the structural evolution. Evolution of structural parameters such as grain boundary contact area and pore radius are controlled by various diffusions mechanisms: surface, grain boundary, and bulk diffusion, which are thermally activated process and have the form:

$$\delta D_s = \delta D_{s_0}\, e^{-(Q_s/RT)},\ \delta D_b = \delta D_{b_0}\, e^{-(Q_b/RT)}, \text{ and } D_V = D_{V_0}\, e^{-(Q_V/RT)}. \tag{29}$$

where Q_s, Q_b and Q_V are the activation energy for surface, grain boundary, and volume diffusion, respectively. δD_{s_0} is the reference surface diffusion times surface layer thickness, δD_{b_0} is the reference grain boundary diffusion times grain boundary thickness, and D_{V_0} is the reference bulk diffusion coefficient.

Grain boundary mobility is also a key structural evolution parameter described by a thermally activated process, as:

$$M_b = M_{b_0}\, e^{-(Q_t/R_g T)}, \tag{30}$$

where Q_t is the activation energy for boundary mobility.

After calculating the strain rate components from Eq. (25) considering Eqs. (26)-(28), they are written in terms of $\Delta\varepsilon^{cr}$ and $\Delta\varepsilon^{sw}$ using Eq. (1). The density increment is given by Eq. (19). Connection between lineal viscosity modulus (K_{lin} in Eq. (26)) and (G_{lin} in Eq. (27)) with the diffusion and mobility coefficients can be found in Ref. [55] and Appendix A.

2.5 *The Kuhn-Sofronis-McMeeking Model*

In this model, the densification has been studied considering creep as the dominant mechanism. Kuhn and McMeeking [22] studied the stage when porosity is open and interconnected with discrete

necks bridging adjacent particles. Sofronis and McMeeking [23] studied the case when pores are closed and isolated from each other. Bhattacharya et al. [21] proposed a connection between Kuhn–McMeeking model (open porosity) and Sofronis–McMeeking model (close porosity). In the present work, we propose a transition assuming that for $\rho = 0.9$, half of the porosity is closed. Close porosity starts to appear for $\rho = 0.85$ and all the pores are closed for $\rho = 0.95$.

The constitutive relations of stage I (open pore) and II (closed pores) are given by

$$ {}_{I}\dot{E}_{ij} = {}_{I}\dot{\varepsilon}\left(\frac{3}{2}a_I \frac{\sigma_{ij}+\sigma_m\delta_{ij}}{q} - \frac{b_I I_{ij}}{3}\right), \tag{31}$$

$$ {}_{II}\dot{E}_{ij} = {}_{II}\dot{\varepsilon}\left(\frac{3}{2}a_{II}(\sigma_{ij}+\sigma_m\delta_{ij}) - \frac{\sigma_m}{3}b_{II} I_{ij}\right), \tag{32}$$

where ${}_{I}\dot{E}_{ij}$ and ${}_{II}\dot{E}_{ij}$ are the components of the creep strain rate tensor of stage I and II, respectively. The dependences for ${}_{I}\dot{\varepsilon}$, a_I and b_I for the KM model, as well as, the functions ${}_{II}\dot{\varepsilon}$, a_{II} and b_{II} are taken from Ref. [21]. Appendix B shows the connection with the temperature-dependent coefficients.

The blending of the two stages is computed by

$$ \dot{\varepsilon}_{ij} = A_{KM}(\rho)\,{}_{I}\dot{E}_{ij} + A_{SM}(\rho)\,{}_{II}\dot{E}_{ij}\,. \tag{33}$$

In Eq. (33), it is expected that ${}_{I}\dot{E}_{ij}$ is dominant when $\rho < 0.9$ and ${}_{II}\dot{E}_{ij}$ when $\rho > 0.9$. Also, $A_{KM}(\rho)$ and $A_{SM}(\rho)$ are the weight coefficients which determine the contributions relative to open and closed porosity for the overall densification. They can be determined as

$$ A_{KM}(\rho) = 1 - f_s(\rho), \tag{34}$$

$$ A_{SM}(\rho) = f_s(\rho), \tag{35}$$

where $f_s(\rho) = b \Big/ \left[1 + e^{-a(\rho - c)}\right]$ with $a = 100$, $b = 1$ and $c = 0.9$.

As in the previous cases, the stress distribution is calculated in the elastic problem, the stress state is imported into the CREEP subroutine in which are implemented the Kuhn-McMeeking and Sofronis-McMeeking densification model [22,23].

After calculating the strain rate components from Eqs. (31) and (32) for each stage, they are written in terms of $\Delta\varepsilon^{cr}$ and $\Delta\varepsilon^{sw}$ using Eq. (1). The density increment is given by Eq. (19).

The temperature dependence of the strain rates for stages I and II (Eqs. (31) and (32)) are described by coefficients A_1 and A_2 (see Appendix B and Ref. [21]):

$$A_1 = A_1^0 \exp\left(-Q_1 / RT\right),\ A_2 = A_2^0 \exp\left(-Q_2 / RT\right), \tag{36}$$

where Q_1 and Q_2 are the activation energy for stage I (Kuhn-McMeeking) and II (Sofronis-McMeeking).

3. MODELS PARAMETERS

For the numerical experiments, three materials were selected: (a) Sodium-borosilicate glass (very similar to Corning glass 7740); b) alumina; and c) zirconia. These materials were chosen because stress-assisted densification data, is available in the literature, for one set of loading conditions for each one of them, as described below.

3.1 *Elastic constitutive behaviors*

The Eqs. (4) and (5) are used to describe the dependence of the elastic properties on porosity for alumina, zirconia and the glass. For alumina, the elastic modulus $\left(E_0\right)$ and the Poisson ratio $\left(\nu_{0p}\right)$ for the fully dense body are assumed equal to 375 GPa and 0.24, respectively [61], and the corresponding values for the glass (Corning glass 7740) are 62.8GPa and 0.20 [62], respectively. For zirconia E_0 and ν_{0p}, values of 220 GPa and 0.27 respectively are used [63].

3.2 *Constitutive parameters for viscous materials*

For the Scherer and SOVS models, two model parameters are needed. They are the reference viscosity, η_0, and the activation energy, Q.

Günay [64] studied the hot-pressing of gel derived and melt derived sodium-borosilicate glass-powder very similar to Corning glass 7740. In the present work, we adjust the Scherer model parameters ($\gamma n^{1/3}$ and viscosity η_0 (given by Eqs. (17) and (18) respectively)) to describe the dependence of the relative density on the sintering time for the gel derived sodium borosilicate glass under uniaxial applied stress of 25MPa at 625ºC and 675ºC. Arhenius temperature

dependence for viscosity (Eq. (18)) is used to fit the experimental data. Good fit was obtained for $\gamma n^{1/3} = 1 J/m^3$, $\eta_0 = 2.48\times10^{-10}\,\mathrm{Pa\cdot s^{-1}}$ and $Q = 290\,KJ\cdot mol^{-1}$.

The SOVS model is also used to describe densification of the same glass powder. The constants a_2, b_2, c_2, a_3, and b_3 are taken from Ref. [44]. Table 3 shows the parameters for Eqs. (23) and (24). The SOVS model density dependence is fitted to the Scherer model density curve by adjusting the reference viscosity to $\eta_0 = 3.78\times10^{-13}\,\mathrm{Pa\cdot s^{-1}}$ and the activation energy $Q = 250\,KJ\cdot mol^{-1}$ following Eq. (18). The difference in the numerical values for the reference viscosity and the activation energy between the "S" and "SOVS" models is a result of the differences in how viscosity has been introduced in the two models. The "S" model is based on the energy balance between surface energy reduction and viscous flow dissipation. The "SOVS" model is based on a continuum phenomenological description.

Table 3. *Skorohod–Olevsky parameters taken from Ref.* [45]. *The radius r is taken from Ref.* [65], *and the surface energy* γ *is an estimation*.

Parameters for the Skorohod – Olevsky model						
a_2	b_2	c_2	a_3	b_3	$r\,(\infty\mathrm{m})$	$\gamma\,(\mathrm{J/cm^2})$
2/3	2.26	1.12	1.7	0.26	8.4	1.0

3.3 *Constitutive parameters for crystalline materials*

Reiterer et al. [65] studied the sinter-forging of Reaction Bonded Alumina (RBAO) with addition of ZrO_2 and 2Y-ZTP, considering the Riedel-Svoboda model. Excellent fit between theoretical and experimental data is reported. The model parameters of Ref. [65] are considered in the present work as the starting values. Then using the experimental results from Ref. [21] on the hot pressing of alumina, the surface, volume, and grain boundary diffusion coefficients, corresponding activation energies (see Eqs. (29)), grain boundary mobility (Eq. (30)) and the interface reaction parameters, α, are adjusted and the best fit values are shown in Table 4. It can be seen that the numbers of parameters to be fitted for the Riedel-Svoboda model is considerably higher than those for the other three models. Therefore, it is possible that different combinations of parameters will provide similar fit to the experimental data. To partially address this, we use physical considerations. Specifically, we consider volume diffusion to have higher activation energy than grain boundary

diffusion which is higher than that for surface diffusion (based on atomic packing considerations). We also consider the interface reaction parameter, α, to be considerably high as reported in Ref. [65] since non-linear effects may appear due to the applied stress. The KSM parameters are also adjusted to experimental data reported by S. Bhattacharya et al. [21] and reported in Table 5. For each sintering stage, only two parameters are needed. They are the reference coefficient A_0 and the thermal activation energy Q_p.

Table 4. *Fitted parameters for the Riedel-Svoboda constitutive law.*

Parameter	Symbol	Pure RBAO
Initial grain size	R_0	0.15 ∝m
External gas pressure	Δp	0.1 MPa
Molecular volume	Ω	1.42×10^{-29} m^3
Grain boundary diffusion	δD_{b_0}	6m^3 / s
	Q_b	475 000 J/mol
Surface diffusion	δD_{s_0}	9×10^{-8} m^3/s
	Q_s	475 000 J/mol
Volume diffusion	D_{V_0}	7.8×10^{-15} m^2/s
	Q_V	800 000 J/mol
Grain boundary mobility	$\gamma_b M_{b_0} / 4$	1.6 m^2/s
	Q_m	572 000 J/mol
Surface energy	γ_s	0.75 J/m^2
Dihedral angle	ψ	60^0
Initial deviation of the Hillert grain size distribution	δ	0
Pore detachment	β_0	1.3
Interface reaction parameter	α	8.25×10^{-7} N

Table 5. *Fitted parameters for the Kuhn-Sofronis-McMeeking model from Ref.* [21] *to match the densification obtained by the RS model for the hot-pressing case with the parameters of Table 4.*

Model	Fitted parameters		
	A_0 (MPa^{-2} s^{-1})	Q_p (KJ mol^{-1})	n
Kuhn-McMeeking	0.0244	133.6	2
Sofronis-McMeeking	6977	284	1

Sinter-forging experimental data, on zirconia, is also selected to be described by the chosen two models. For this case II, density, as a function of time for zirconia powder, reported by K.T. Kim et al. has been used [26]. Table 6 reports fitted parameters for the Riedel-Svoboda model and Table 7 shows the fitted parameters for the Kuhn-Sofronis-McMeeking model. The sinter-forging experiment reported in Ref. [26] is an isothermal case for T = 1300°C. Therefore, the activation energies for diffusion coefficients cannot be obtained. Hence, the fitted RS parameters are: grain boundary diffusion, δD_b, surface diffusion, δD_s, and volume diffusion, D_V; and for the KSM model are: A_1 and A_2. K.T. Kim et al. [26] reports grain size as a function of time and this dependence is included in the RS model. Therefore, grain boundary mobility considered in the RS model does not have to be fitted.

Table 6. *Fitted parameters for the Riedel-Svoboda constitutive law.*

Parameter	Symbol	Pure RBAO
Initial grain size	R_0	0.15 ∝m
External gas pressure	Δp	0.1 MPa
Molecular volume	Ω	1.42×10^{-29} m^3
Grain boundary diffusion	δD_b	1.192×10^{-18}m^3 / s
Surface diffusion	δD_s	1.52×10^{-23} m^3/s
Volume diffusion	D_V	6.85×10^{-11} m^2/s
Surface energy	γ_s	0.75 J/m^2
Dihedral angle	ψ	55^0
Initial deviation of the Hillert grain size distribution	δ	0
Pore detachment	β_0	2.0
Interface reaction parameter	α	1.0×10^{-14} N

Table 7. *Fitted parameters for the Kuhn-Sofronis-McMeeking model from Ref.* [21] *to match the densification obtained by the RS model for the hot-pressing case with the parameters of Table 4.*

Model	Fitted parameters	
	A (MPa^{-2} s^{-1})	n
Kuhn-McMeeking	3.86×10^{-6}	2
Sofronis-McMeeking	6.71×10^{-6}	1

4. RESULTS AND DISCUSSIONS

4.1 Isothermal Hot-pressing and Sinter-forging

Fig. 3 shows the dependence of the relative density on time considering the Scherer cell model and the Skorohod – Olevsky model for two different temperatures T = 625°C and 675°C, for sodium-borosilicate glass. Figs. 3(a) and 3(b) illustrate case I (hot-pressing) and case II (sinter-forging), respectively. It can be seen in Fig. 3(a) that both the Scherer (S) and the Skorohod–Olevsky (SOVS) models can be used to fit the experimental results for two temperatures and get the needed constitutive parameters. These parameters can be used to predict densification at a different hot-pressing temperature. As can be observed, the predictions of the Scherer and the Skorohod–Olevsky models are very close to each other and in good agreement with experimental data [64].

Fig. 3(b) depicts the density as a function of time for sinter-forging (case II) with the model parameters that were obtained from the hot-pressing case (case I). It can be observed that the difference between Sherer and SOVS models for 625°C is small. However, as the temperature increases, for 675° C, this difference becomes more noticeable reaching a maximum relative difference of about 6%. Since experimental results are not available for his case, it is not possible to say which model is better. According to the model considerations, the densification behavior is a result of the combined effect of the thermal dependence of viscosity and the stress state during sintering.

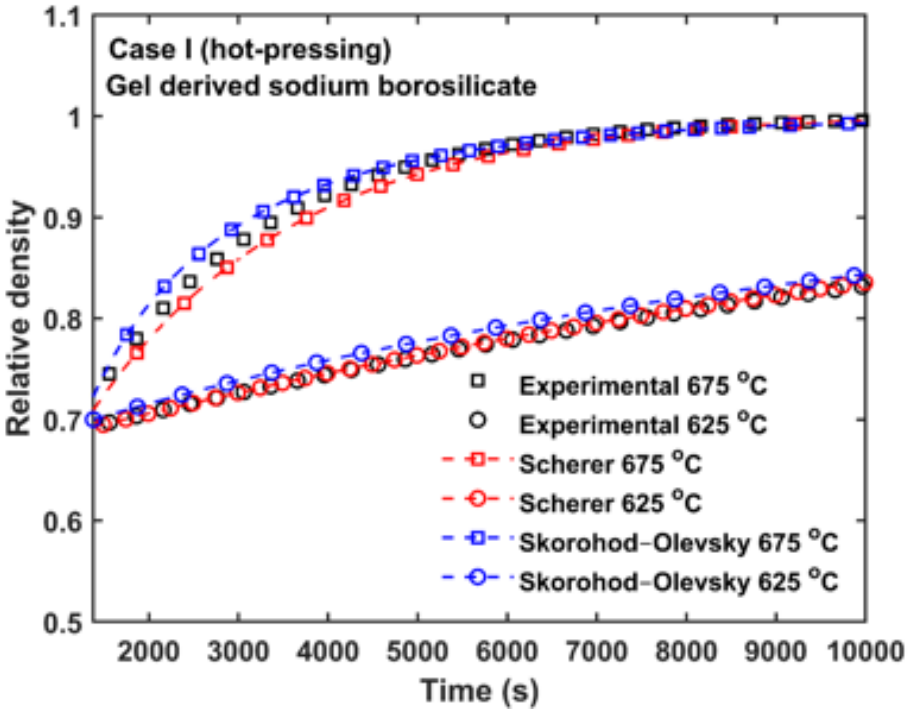

Fig. 3(a). *Dependence of the relative density on the sintering time for amorphous powder compact for case I (hot-pressing). Lines with squared markers correspond to the temperature T* = 675 ºC; *lines with circular markers to T* = 625 ºC. *The experimental results are for hot-pressing of gel derived sodium borosilicate at* 25 MPa *considering* 675 ºC *and* 625 ºC [65].

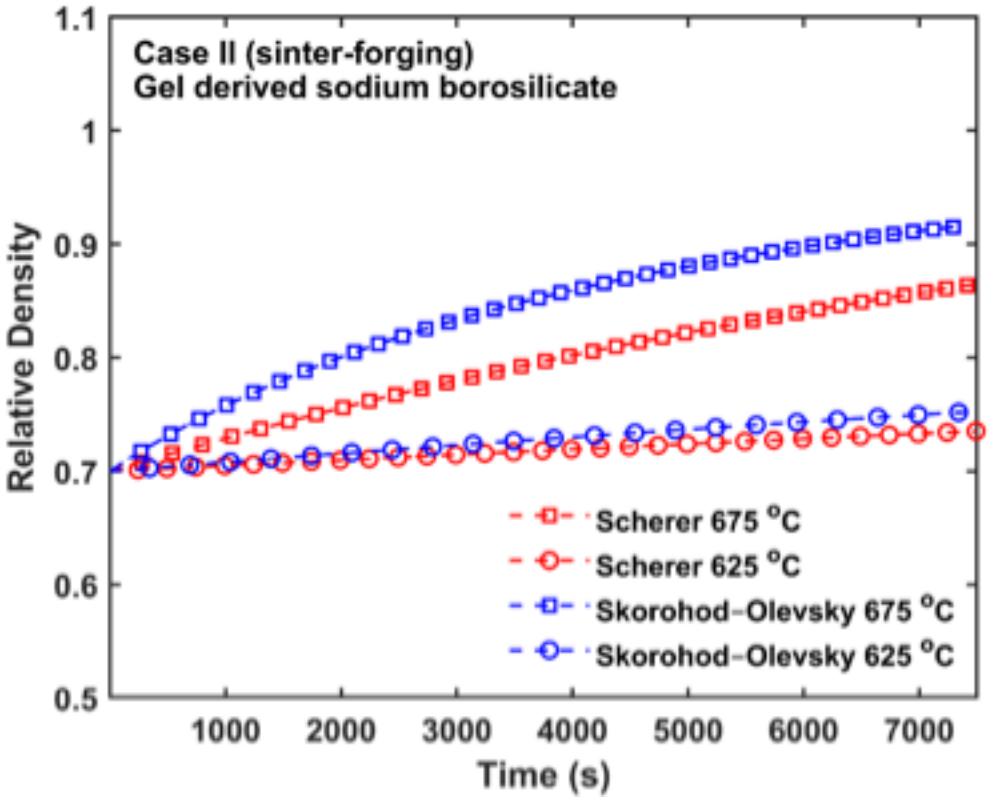

Fig. 3(b). *Predicted dependence of the relative density on the sintering time for amorphous powder compact for case II (sinter-forging). Lines with squared markers correspond to the temperature T* = 675 ºC*; lines with circular markers to T* = 625 ºC. *The uniaxial stress for sinter-forging is* 10 MPa.

Figure 3 clearly shows the effect of the state of the stress on the densification. As can be seen, the densification under hot-pressing conditions is higher than under sinter-forging conditions. This is primarily due to the higher level of uniaxial stress for the hot-pressing. An additional effect is that due to die confinement in hot-pressing, the hydrostatic compressive stress is higher (for the same applied uniaxial stress). The hydrostatic compressive stress is the driving force for enhanced densification in stress-assisted sintering.

Fig. 4 shows the densification dependences for crystalline materials considering the Riedel–Svoboda model and the Kuhn–Sofronis–McMeeking model for the temperatures T equals to 1400º C and 1450º C. Fig. 4(a) is obtained using the RS model for the fitted parameters reported in Table 4 under isothermal conditions. For the KSM model, the parameters listed in Table 5 were used. As

can be seen, good fit is obtained for both temperatures between the experimental results and the RS and KSM model predictions. We then use these parameters to predict the densification during sinter-forging. As can be observed in Fig. 4(b), the densification behavior described by KSM and RS is similar with a maximum relative difference of about 6%. Since experimental results are not available for his case, it is not possible to say which model is better.

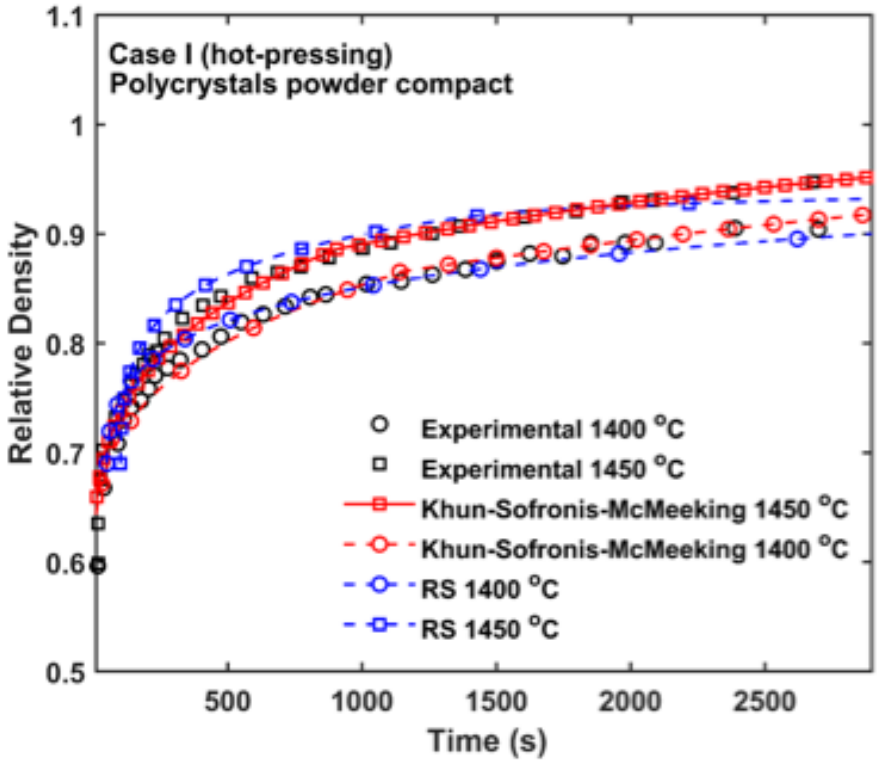

Fig. 4(a). *Dependence of the relative density on the sintering time for Alumina polycrystals powder compact for case I (hot-pressing). Lines with squared markers correspond to the temperature T =* 1450°C; *lines with circular markers to T =* 1400°C. *For both models, the hot-pressing stress is* 10 MPa.

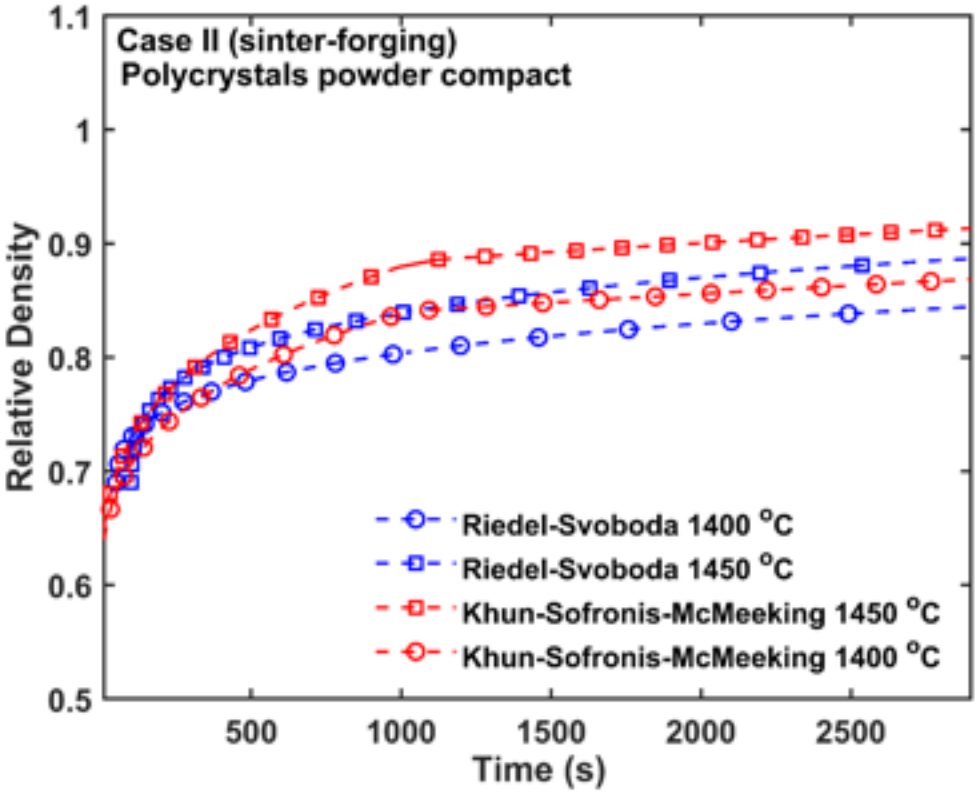

Fig. 4(b). *Predicted dependence of the relative density on the sintering time for Alumina polycrystals powder compact for case II (sinter-forging). Lines with circular markers correspond to the temperature* T = 1400ºC; *lines with squared markers to* T = 1450ºC. *The sinter-forging stress is* 10 MPa.

As for amorphous materials, Figure 4 also clearly shows the effect of the state of the stress on the densification. The densification under hot-pressing conditions is higher than under sinter-forging conditions, for the same applied axial stress. This is due to the die confinement in hot-pressing leading to higher hydrostatic compressive stresses which is the driving force for enhanced densification in stress-assisted sintering.

In Figure 5, we plot the density as a function of time for zirconia powder compact during sinter-forging at two different stresses and one temperature. The experimental results and the predictions of the RS and KSM models are presented. It can be seen that the RS model predicts the density quite well up to about 0.95 relative density. The model over estimates the density beyond 0.95

relative density. This difference maybe due to factors not considered in the model (e.g., friction between the sample and the piston leading to barreling of the sample). For high enough stress values, cracks can be also observed at the cylindrical faces.

It can be also observed that, a good fitting is obtained for P = 8.8 MPa for the Kuhn–Sofronis–McMeeking (KSM) model. However, when the applied stress is P = 17.9 MPa, the KSM model prediction is not as good. The possibilities to improve this result are low because only few parameters are needed for the KSM model as seen in Table 7. To better understand this result, it is useful to recall that RS model is based on the physical mechanics of sintering and the KSM model is a phenomenological description. Hence, it is possible to conclude that RS model provides a more realistic description. However, a possible disadvantage is the large number of parameters to be found. Finally, Fig. 5(b) reports the dependence of relative density as a function of time for hot pressing. It can be seen that the predictions of the RS model and KSM model are different. The reason is the above-mentioned differences between these two models.

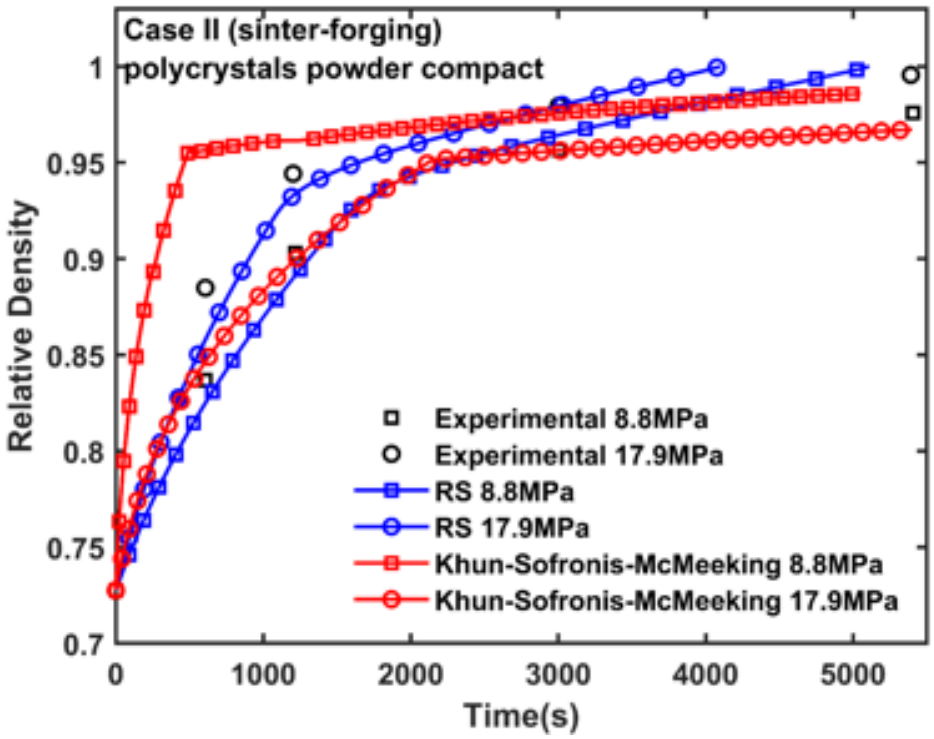

Fig. 5(a). *Dependence of the relative density on the sintering time for Zirconia polycrystals powder compact for case II (snter-forging). Lines with squared markers correspond to the applied stress* P = 8.8 MPa; *lines with circular markers to* P = 17.9 MPa. *For both cases, the temperature is equal to* 1300ºC.

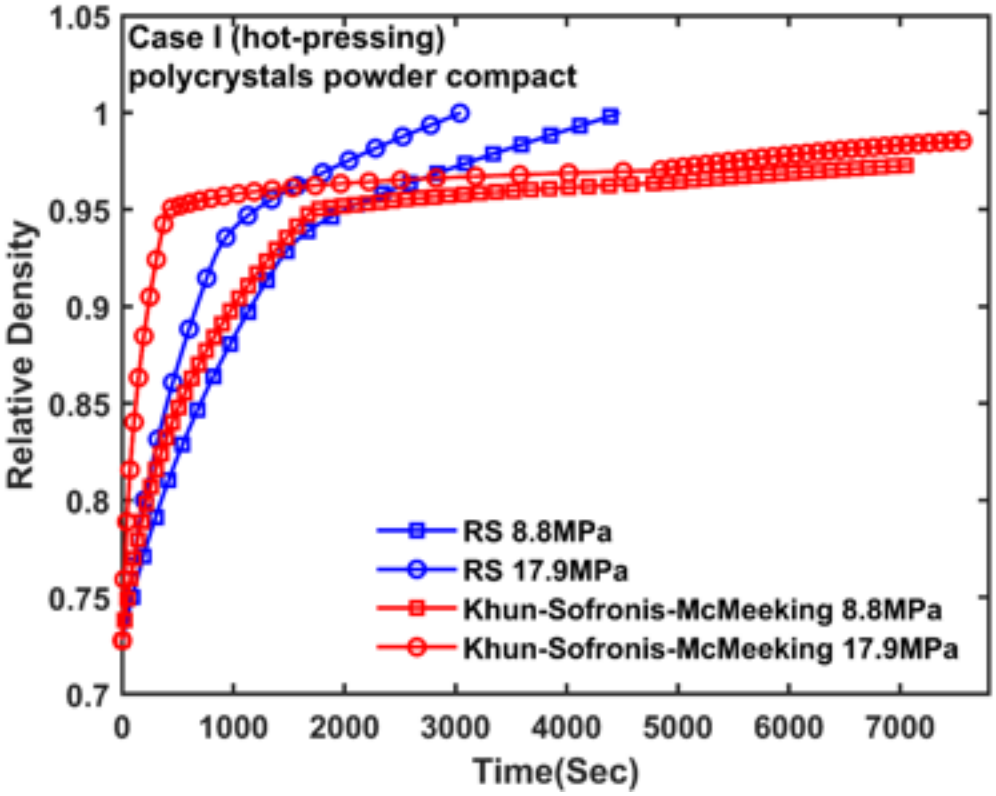

Fig. 5(b). *Dependence of the relative density on the sintering time for Zirconia polycrystals powder compact for case I (hot pressing). Lines with squared markers correspond to the applied stress P* = 8.8 MPa; *lines with circular markers to P* = 17.9 MPa. *For both cases, the temperature is equal to* 1300ºC.

Figure 5 clearly shows the effect of the level of applied stresses. As expected, for both sinter-forging and hot pressing, the densification increases as the stress level increases.

4.2 Constant Heating Rate Hot-pressing

Densification under constant heating rates is also of interest. Due to the different nature of the materials, i.e., amorphous, and crystalline, the temperature change needs to be normalized. In Fig. 6, the relative density is plotted as a function of homologous temperature for two heating rates equal to 10 K/min and 15 K/min for the case I, i.e., hot-pressing. Homologous temperature is defined as T/T_r, where T_r is a reference temperature (in Kelvin) taken as the glass transition temperature, T_f, for glasses and the melting temperature, T_m, for ceramics. For borosilicate

(Corning glass 7740) the glass transition temperature is reported to be 1525 K. The melting point for alumina we use the known melting point of 2233 K.

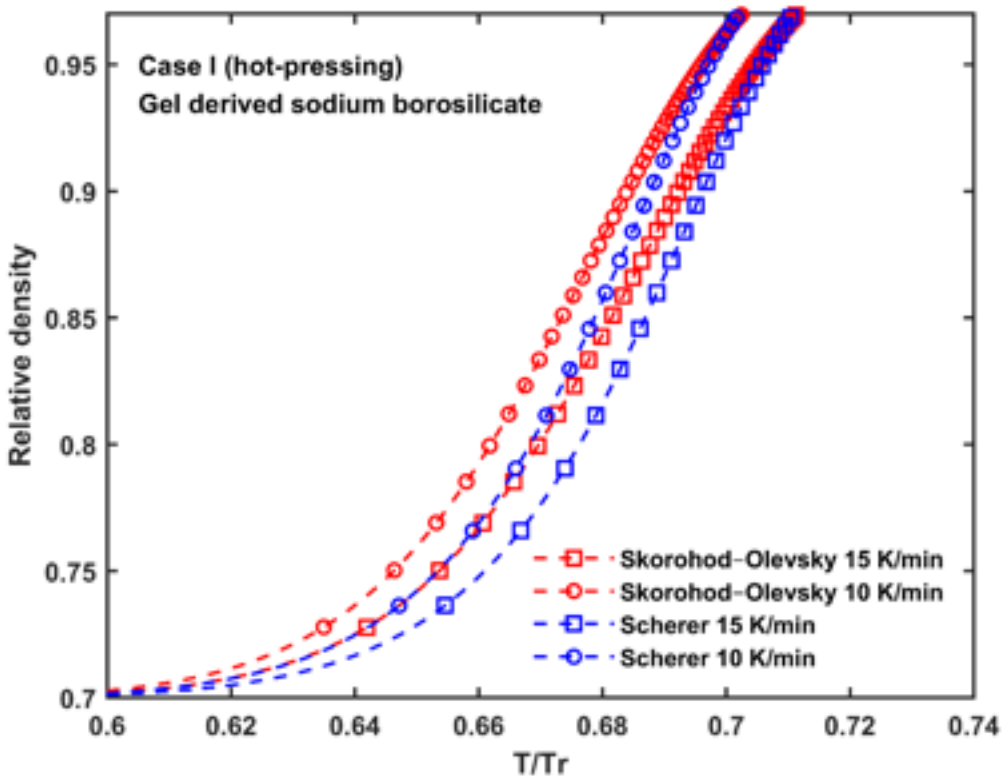

Fig. 6(a). *Relative density as function of homologous temperature for amorphous powder compact for case I (hot-pressing) at different heating rates*.

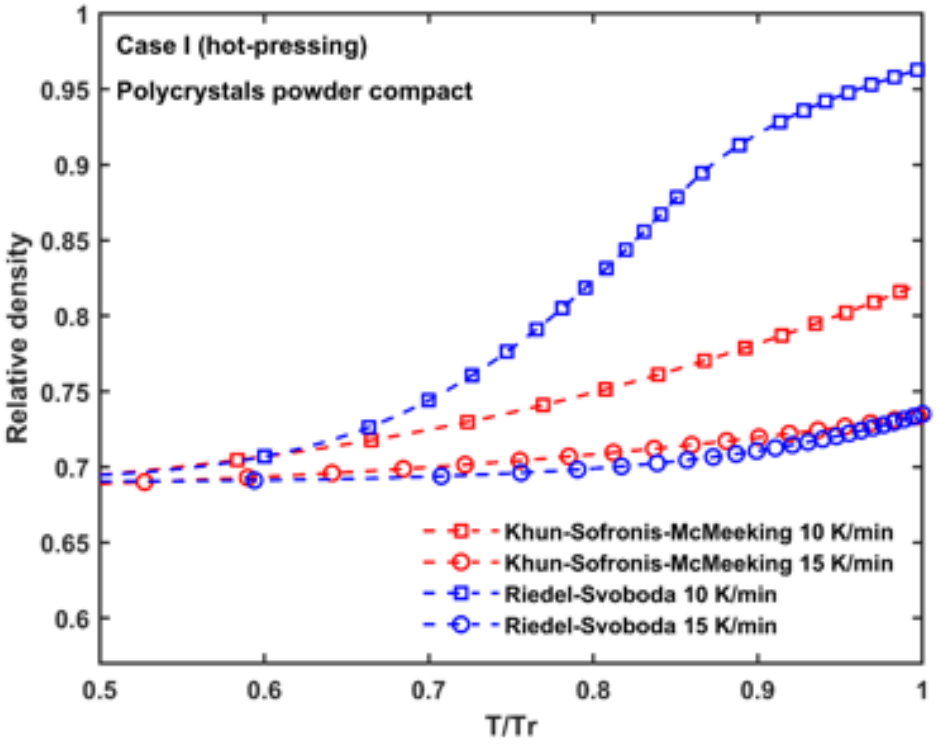

Fig. 6(b). *Relative density as function of homologous temperature for polycrystalline ceramics powder for case I (hot-pressing) at different heating rates*.

For amorphous materials, hot-pressed at constant heating rate (Figure 6(a)), it can be observed that the predictions of both SOVS and Scherer models are quite similar. This is expected since their predictions for the isothermal hot-pressing are similar and both of them have only one temperature dependent parameter, viscosity, which has identical Arrhenius dependences.

In contrast, as seen in Fig. 6(b), for crystalline materials, the RS model is more sensitive to the change in the heating rate than the KSM model. This may be because the RS constitutive model involves the activation of several mechanisms and their statistical weight changes as temperature changes. On the other hand, KSM considers creep as the only one thermally activated process. Both models predict density dependences close to each other for heating rate = 15 K/min. However, for heating rate = 10 K/min, the difference between predictions is considerable and becomes even larger as the temperature increases. Experimental data will be needed to identify which model can provide the better prediction.

CONCLUSIONS

In the literature, different constitutive laws have been proposed and used to investigate stress-assisted sintering. In this work, we have investigated, numerically, the predictions of the densification behavior using four commonly used constitutive laws (two for polycrystalline ceramics and two for amorphous) for two stress assisted sintering cases: hot-pressing and sinter-forging temperature. The following conclusions can be drawn from this study:

1. Using experimental data from isothermal hot pressing to obtain the constitutive parameters, the response of the two models for amorphous materials, the Scherer and the Skorohod–Olevsky models, is quite similar and matches the experimental results well. However, when the same parameters are used to predict the densification during sinter-forging, the match between models is sensitivity to temperature. For example, for 625 ^{o}C, the densification behaviors described by Scherer and Skorohod–Olevsky are close to each other, but, at 675 ^{o}C, there is significant difference between the two models reaching as high as 6% of relative density difference.
2. For crystalline material using experimental data from isothermal hot pressing to obtain the constitutive parameters, the two models, the Riedel–Svoboda and the Kuhn–Sofronis–McMeeking predict similar densification response at two different temperatures for the hot-pressing case. However, when the same parameters are used to predict the densification during sinter-forging, the match between models is not as good with the difference reaching as high as 5% of relative density difference.
3. Experimental data from a sinter-forging Zirconia powder compact allows finding fitted parameters that provides a good description for polycrystals materials considering the Riedel–Svoboda model, but, for density values higher than 95%, a discrepancy can be observed for both applied stresses. The Kuhn–Sofronis–McMeeking model can provide a good description for P = 8.8 MPa, but not for P = 17.9 MPa. This leads us to conclude that RS model is better for polycrystalline ceramics.
4. Using isothermal hot-pressing to obtain constitutive parameters and applying them to constant heating rate hot-pressing at different heating rate, the Scherer and the Skorohod–Olevsky model have almost identical predictions. However, the predictions are quite different for the case of RS and KSM models.

The overall conclusion is that for amorphous materials, parameters can be obtained using one set of experiments (e.g., isothermal hot pressing) and applied to a different loading and thermal history and the two models give comparable results. The exception is the large difference between models for the case of sinter-forging at 675 ºC. The reasons for this are not clear. On the other hand, for crystalline materials, good fits are only obtained when the model is applied to the loading and thermal history under which parameters have been obtained. This is rather limiting for a general model. Additional research needs to be conducted to densify crystalline materials under a broader set of loading and thermal history and constitutive parameters extracted under these different conditions. A comparison between these constitutive parameters will be illustrative of the range of conditions under which the models can be used.

ACKNOWLEDGEMENT

IMEA would like to thank CONACYT – PNPC for the Ph.D. scholarship to develop this work. HCM is grateful for the support of the CONACYT Basic Science Grants A1-S-9232. YEA gratefully acknowledges the financial support of the Grant SEP CB 17-18 A1-S-37066 during the postdoctoral stay 2021 – 2022 at Universidad Autónoma de Ciudad Juárez. RKB acknowledges partial support from NSF DMREF grant No. 2119833.

DECLARATIONS

Conflict of interest: The authors declare that they have no conflict of interest.

APPENDIX A

Eqs. (26) and (27) shows the relation of the bulk and shear viscosities with the linear coefficients:

$$K_{lin} = \frac{kTr^3}{\Omega \delta D_b}\left(\left(1-\theta\right)k_1 + \theta k_2\right)U$$

$$G_{lin} = \frac{kTr^3}{\Omega \delta D_b}\left(\left(1-\theta\right)g_1 + \theta g_2\right)U$$

where k_1, k_2, g_1, and g_2 are defined as normalized bulk viscosity and shear viscosity. They depend on the relations: $\delta D_b / \delta D_s$ and $\delta D_b / \delta D_v$ as can be seen in Ref. [55] and can be described as thermal activated process according to Eq. (29).

The evolution of grain size, r, is also a thermal activated process that can be described by the relation:

$$\dot{r} = \frac{\gamma_b M_b}{4r} \frac{F_d}{F_p}$$

F_d and F_p are factors that describe the deviation from the classical Hillert law as reported in Ref. [55]. F_d accounts for the fact that the powder usually does not have the steady-state grain size distribution. F_p arises from the drag that pores exert on migrating grain boundaries. Further details can be seen in Ref. [55]. Grain boundary mobility, M_b, is also a thermal activated process following the Eq. (30).

APPENDIX B

Eqs. (31) and (32) depends on ${}_I\dot{\varepsilon}$ and ${}_{II}\dot{\varepsilon}$ respectively. ${}_I\dot{\varepsilon}$ are related to A_1 and ${}_I\dot{\varepsilon}$ to A_1 as can be seen in Eqs.

$${}_I\dot{\varepsilon} = \frac{2}{3} C_{cr} \left[\left|\sigma_m\right|^{(n_1+1)/n_1} + \left(\frac{2q}{3}\right)^{(n_1+1)/n_1} \right]^{n_1-1} \times \left[\frac{1}{2}\left|\sigma_m\right|^{2/n_1} + \left(\frac{2q}{3}\right)^{2/n_1} \right]^{1/2}$$

$$C_{cr} = A_1 \frac{27\pi}{16\times 3^{1/2}} \frac{\left(1-\rho_0\right)^{n_1-0.5}\left(\rho-\rho_0\right)^{0.5}}{\left[3\rho^2\left(\rho-\rho_0\right)\right]^{n_1}}$$

$${}_{II}\dot{\varepsilon} = A_2\left(a_{II}q^2 + b_{II}{\sigma_m}^2\right)^{(n_2-1)/2}$$

The parameters a_I, b_I, a_{II} and b_{II} are functions of p and σ_m as reported in Ref. [21]. A_1 and A_2 describe thermal activated process as observed in Eqs. (36).

REFERENCES

1. Li W-B, Ashby MF, Easterling KE. On densification and shape change during hot isostatic pressing. Acta Metall. 1987;35(12):2831–42. https://doi.org/10.1016/0001-6160(87)90282-3
2. Winnubst AJA, Boutz MMR. Sintering and densification; new techniques: sinter forging. Key Eng Mater. 1998; 153-154: 301-323. https://inis.iaea.org/search/29054013
3. German RM. Chapter Ten - Sintering With External Pressure. In: German RMBT-S from EO to SP, editor. Boston: Butterworth-Heinemann; 2014. p. 305–54. https://doi.org/10.1016/B978-0-12-401682-8.00010-0

4. Zuo R, Aulbach E, Bordia RK, Rödel J. Critical Evaluation of Hot Forging Experiments: Case Study in Alumina. J Am Ceram Soc. 2003;86(7):1099–105. https://doi.org/10.1111/j.1151-2916.2003.tb03431.x
5. Hague DC, Mayo MJ. Sinter-Forging of Nanocrystalline Zirconia: I, Experimental. J Am Ceram Soc. 1997;80(1):149–56. https://doi.org/10.1111/j.1151-2916.1997.tb02803.x
6. Hague DC, Mayo MJ. Sinter-Forging of Nanocrystalline Zirconia: II, Simulation. J Am Ceram Soc. 1999;82(3):545–55. https://doi.org/10.1111/j.1151-2916.1999.tb01799.x
7. Kondo N, Asayama M, Suzuki Y, Ohji T. High-Temperature Strength of Sinter-Forged Silicon Nitride with Lutetia Additive. J Am Ceram Soc. 2003;86(8):1430–2. https://doi.org/10.1111/j.1151-2916.2003.tb03489.x
8. Kim H-E, Moorhead AJ. Optical and Mechanical Properties of Hot-Pressed Cesium Iodide. J Am Ceram Soc. 1990;73(3):496–501. https://doi.org/10.1111/j.1151-2916.1990.tb06544.x
9. Song K-H, Sorrell CC, Dou S-X, Liu H-K. Effect of Hot-Pressing on the Bi─Pb─Sr─Ca─Cu─O System. J Am Ceram Soc. 1991;74(10):2577–82. https://doi.org/10.1111/j.1151-2916.1991.tb06802.x
10. Ostrowski T, Rödel J. Evolution of Mechanical Properties of Porous Alumina during Free Sintering and Hot Pressing. J Am Ceram Soc. 1999;82(11):3080–6. https://doi.org/10.1111/j.1151-2916.1999.tb02206.x
11. Kimura T, Yoshimoto T, Iida N, Fujita Y, Yamaguchi T. Mechanism of Grain Orientation During Hot-Pressing of Bismuth Titanate. J Am Ceram Soc. 1989;72(1):85–9. https://doi.org/10.1111/j.1151-2916.1989.tb05958.x
12. Ghassemi Kakroudi M, Dehghanzadeh Alvari M, Shahedi Asl M, Pourmohammadie Vafa N, Rabizadeh T. Hot pressing and oxidation behavior of ZrB2–SiC–TaC composites. Ceram Int. 2020;46(3):3725–30. https://doi.org/10.1016/j.ceramint.2019.10.093
13. Foong LK, Xu C. Hot pressing and microstructural characterization of SiC and TiN added TiB2 ceramics. Ceram Int. 2021;47(3):3946–54. https://doi.org/10.1016/j.ceramint.2020.09.258
14. Nguyen V-H, Delbari SA, Shahedi Asl M, Sabahi Namini A, Ghassemi Kakroudi M, Azizian-Kalandaragh Y, et al. Role of hot-pressing temperature on densification and microstructure of ZrB2–SiC ultrahigh temperature ceramics. Int J Refract Met Hard Mater. 2020;93:105355. https://doi.org/10.1016/j.ijrmhm.2020.105355
15. Yang X, Guo Y, Han Y, Li Y, Ma T, Chen M, et al. Significant improvement of thermal conductivities for BNNS/PVA composite films via electrospinning followed by hot-pressing technology. Compos Part B Eng. 2019;175:107070. https://doi.org/10.1016/j.compositesb.2019.107070
16. Guillon O. Effects of Applied Stress and Heating Rate in Field Assisted Sintering. In: Castro Ricardoand van Benthem K, editor. Sintering: Mechanisms of Convention Nanodensification and Field Assisted Processes. Berlin, Heidelberg: Springer Berlin Heidelberg; 2013. p. 195–213. Available from: https://link.springer.com/chapter/10.1007/978-3-642-31009-6_9

17. Amaral L, Jamin C., Senos A.M.R., Vilarinho P.M., Guillon O. Constrained sintering of BaLa4Ti4O15 thick films: Pore and grain anisotropy. Journal of the European Ceramic Society, 2013; 33(10): 1801-1808 https://doi.org/10.1016/j.jeurceramsoc.2013.01.031.
18. Hernandez-Cuevas G, Leyva Mendoza JR, García-Casillas PE, Rodríguez González CA, Hernandez-Paz JF, Herrera-Pérez G, et al. Effect of the sintering technique on the ferroelectric and d33 piezoelectric coefficients of Bi0.5(Na0.84K0.16)0.5TiO3 ceramic. J Adv Ceram. 2019;8(2):278–88. https://doi.org/10.1007/s40145-019-0314-8
19. Riedel H, Meyer D, Svoboda J, Zipse H. Numerical simulation of Die pressing and sintering: development of constitutive equations. Int J Refract Met Hard Mater. 1993;12:55–60. https://doi.org/10.1016/0263-4368(93)90016-9
20. Scherer GW. Viscous Sintering under a Uniaxial Load. J Am Ceram Soc. 1986;69(9):C-206-207. https://doi.org/10.1111/j.1151-2916.1986.tb07479.x
21. Bhattacharya S, Jakus K, Grosse I. Modelling pressure-assisted densification by power-law creep. J Mater Sci. 1997;32(23):6183–9. https://doi.org/10.1023/A:1018668606955
22. Kuhn LT, McMeeking RM. Power-law creep of powder bonded by isolated contacts. Int J Mech Sci. 1992;34(7):563–73. https://doi.org/10.1016/0020-7403(92)90031-B
23. Sofronis P, McMeeking RM. Creep of Power-Law Material Containing Spherical Voids. J Appl Mech. 1992;59(2S):S88–95. https://doi.org/10.1115/1.2899512
24. Chung SH, Kwon YS, Hyun CM, Kim KT, Kim MJ, German RM. Analysis and Design of a Press-and-Sinter Process for Fabrication of Precise Tungsten Carbide Cutting Tools. In: Advances in Powder Metallurgy and Particulate Materials. 2004. p. 26–39. Available from: https://citeseerx.ist.psu.edu/viewdoc/summary?doi=10.1.1.563.8494
25. Hague DC, Mayo MJ. Modeling densification during sinter-forging of yttria-partially-stabilized zirconia. Mater Sci Eng A. 1995;204(1):83–9. https://doi.org/10.1016/0921-5093(95)09942-5
26. Kim K, Kim HG, Jang HM. Densification behavior and grain growth of zirconia powder compact under high temperature. Int J Eng Sci. 1998;36:1295–312. https://doi.org/10.1016/S0020-7225(98)00016-0
27. Wakai F, Okuma G, Mücke R, Guillon O. Modelling of elimination of strength-limiting defects by pressure-assisted sintering at low stress levels. J Eur Ceram Soc. 2021; 41(16): 202 – 210. https://doi.org/10.1016/j.jeurceramsoc.2021.09.040
28. Braginsky M, Tikare V, Olevsky E. Numerical simulation of solid state sintering. International journal of solids and structures. 2005 Jan 1;42(2):621-36. https://doi.org/10.1016/j.ijsolstr.2004.06.022
29. Van Nguyen C, Deng Y, Bezold A, Broeckmann C. A combined model to simulate the powder densification and shape changes during hot isostatic pressing. Comput Methods Appl Mech Eng. 2017;315:302–15. https://doi.org/10.1016/j.cma.2016.10.033
30. Rybakov KI, Olevsky EA, Krikun EV. Microwave sintering: fundamentals and modeling. Journal of the American Ceramic Society. 2013 Apr;96(4):1003-20. https://doi.org/10.1111/jace.12278
31. Olevsky E, Froyen L. Constitutive modeling of spark-plasma sintering of conductive materials. Scripta materialia. 2006 Dec 1;55(12):1175-8. https://doi.org/10.1016/j.scriptamat.2006.07.009

32. Yin Z, Ye J, Hong D, Xu W. Effect of molding pressure on structural and densification behavior of microwave-sintered ceramic tool material. Int J Appl Ceram Technol. 2019;16(5):2085–93. https://doi.org/10.1111/ijac.13237
33. Bouvard D. Modelling the densification of powder composites by power law creep. Acta Metall Mater. 1993;41(5):1413–20. https://doi.org/10.1016/0956-7151(93)90250-V
34. Kim HG, Gillia O, Bouvard D. A phenomenological constitutive model for the sintering of alumina powder. J Eur Ceram Soc. 2003;23(10):1675–85. https://doi.org/10.1016/S0955-2219(02)00411-9
35. Bouvard D, Martin CL. Micromechanical modelling of powder sintering. In: Kishino Y, editor. Powders and Grains 2001. 1st ed. London: CRC Press; 2020. p. 47–50. Available from: https://www.taylorfrancis.com/chapters/edit/10.1201/9781003077497-147/micromechanical-modelling-powder-sintering-bouvard-martin
36. Rahaman MN, De Jonghe LC. Sintering of CdO Under Low Applied Stress. J Am Ceram Soc. 1984;67(10):C-205-C-207. https://doi.org/10.1111/j.1151-2916.1984.tb19665.x
37. Rahaman MN, De Jonghe LC, Brook RJ. Effect of Shear Stress on Sintering. J Am Ceram Soc. 1986;69(1):53–8. https://doi.org/10.1111/j.1151-2916.1986.tb04693.x
38. Jagota A, Mikeska KR, Bordia RK. Isotropic constitutive model for sintering particle packings. Journal of the American Ceramic Society. 1990 Aug;73(8):2266-73. https://doi.org/10.1111/j.1151-2916.1990.tb07587.x
39. Panda PC, Wang J, Raj R. Sinter-Forging Characteristics of fine-Grained Zirconia. J Am Ceram Soc. 1988;71(12):C-507-C-509. https://doi.org/10.1111/j.1151-2916.1988.tb05820.x
40. Bordia RK, Scherer GW. On constrained sintering—I. Constitutive model for a sintering body. Acta Metall. 1988;36(9):2393–7. https://doi.org/10.1016/0001-6160(88)90189-7
41. Bordia RK, Scherer GW. On constrained sintering—II. Comparison of constitutive models. Acta Metall. 1988;36(9):2399–409. https://doi.org/10.1016/0001-6160(88)90190-3
42. Coble RL. Diffusion Models for Hot Pressing with Surface Energy and Pressure Effects as Driving Forces. J Appl Phys. 1970;41(12):4798–807. https://doi.org/10.1063/1.1658543
43. Camacho-Montes H, García-Casillas PE, Rodríguez-Ramos R, Fuentes-Montero ME, Fuentes-Cobas LE. Simulation of the Stress-Assisted Densification Behavior of a Powder Compact: Effect of Constitutive Laws. J Am Ceram Soc. 2008;91(3):836–45. https://doi.org/10.1111/j.1551-2916.2007.02219.x
44. Reiterer MW, Ewsuk KG. An Analysis of Four Different Approaches to Predict and Control Sintering. J Am Ceram Soc. 2009;92(7):1419–27. https://doi.org/10.1111/j.1551-2916.2009.03009.x
45. Svoboda J, Riedel H, Zipse H. Equilibrium pore surfaces, sintering stresses and constitutive equations for the intermediate and late stages of sintering—I. computation of equilibrium surfaces. Acta Metall Mater. 1994;42(2):435–43. https://doi.org/10.1016/0956-7151(94)90498-7
46. Riedel H, Zipse H, Svoboda J. Equilibrium pore surfaces, sintering stresses and constitutive equations for the intermediate and late stages of sintering—II. Diffusional

densification and creep. Acta Metall Mater. 1994;42(2):445–52. https://doi.org/10.1016/0956-7151(94)90499-5
47. Olevsky EA. Theory of sintering: from discrete to continuum. Mater Sci Eng R Reports. 1998;23(2):41–100. https://doi.org/10.1016/S0927-796X(98)00009-6
48. Bordère S. Original Monte Carlo Methodology Devoted to the Study of Sintering Processes. J Am Ceram Soc. 2002;85(7):1845–52. https://doi.org/10.1111/j.1151-2916.2002.tb00363.x
49. Sutton RA, Schaffer G. An atomistic simulation of solid state sintering using Monte Carlo methods. Mater Sci Eng A-structural Mater Prop Microstruct Process. 2002;335:253–9. https://doi.org/10.1016/S0921-5093(01)01939-6
50. Su H, Johnson DL. Master Sintering Curve: A Practical Approach to Sintering. J Am Ceram Soc. 1996;79(12):3211–7. https://doi.org/10.1111/j.1151-2916.1996.tb08097.x
51. Hansen JD, Rusin RP, Teng M-H, Johnson DL. Combined-Stage Sintering Model. J Am Ceram Soc. 1992;75(5):1129–35. https://doi.org/10.1111/j.1151-2916.1992.tb05549.x
52. Kiani S, Pan J, Yeomans JA. A new scheme of finding the master sintering curve. Journal of the American Ceramic Society. 2006 Nov;89(11):3393-6. https://doi.org/10.1111/j.1551-2916.2006.01252.x
53. Bordia RK, Kang S-JL, Olevsky EA. Current understanding and future research directions at the onset of the next century of sintering science and technology. J Am Ceram Soc. 2017;100:2314–52. https://doi.org/10.1111/jace.14919
54. Skorokhod V V. Rheological Bases of Sintering Theory [in Russian]. Kiev: Nauk. Dumka; 1972.
55. Kraft T, Riedel H. Numerical simulation of solid state sintering; model and application. J Eur Ceram Soc. 2004;24(2):345–61. https://doi.org/10.1016/S0955-2219(03)00222-X
56. Scherer GW. Cell Models for Viscous Sintering. J Am Ceram Soc [Internet]. 1991 Jul 1;74(7):1523–31. Available from: https://doi.org/10.1111/j.1151-2916.1991.tb07135.x
57. USDFLD [Internet]. [cited 2021 Sep 23]. https://abaqus-docs.mit.edu/2017/English/SIMACAESUBRefMap/simasub-c-usdfld.htm#simasub-c-usdfld
58. CREEP [Internet]. [cited 2021 Sep 23]. https://abaqus-docs.mit.edu/2017/English/SIMACAESUBRefMap/simasub-c-creep.htm
59. Roberts AP, Garboczi EJ. Elastic Properties of Model Porous Ceramics. J Am Ceram Soc. 2000;83(12):3041–8. https://doi.org/10.1111/j.1151-2916.2000.tb01680.x
60. Mackenzie JK, Shuttleworth R. A Phenomenological Theory of Sintering. Proc Phys Soc Sect B. 1949;62(12):833–52. http://dx.doi.org/10.1088/0370-1301/62/12/310
61. Flinn BD, Bordia RK, Zimmermann A, Rödel J. Evolution of defect size and strength of porous alumina during sintering. J Eur Ceram Soc. 2000;20(14):2561–8. https://doi.org/10.1016/S0955-2219(00)00133-3
62. Soda Borosilicate (7740) [Internet]. [cited 2021 Sep 23]. https://www.corning.com/media/worldwide/csm/documents/fiches Verre pour poudre 7740.pdf

63. Adams JW, Ruh R, Mazdiyasni KS. Young's Modulus, Flexural Strength, and Fracture of Yttria-Stabilized Zirconia versus Temperature. J. Am. Ceram. Soc. 1997; 80(4) 903–8. https://doi.org/10.1111/j.1151-2916.1997.tb02920.x
64. Günay V. Hot-pressing behaviours of the gel and melt-derived sodium-borosilicate glass powders. Ceram Int. 1997;23(4):291–6. https://doi.org/10.1016/S0272-8842(96)00010-7
65. Réitérer M, Kraft T, Riedel H. Application of a Microstructure-Based Model for Sintering and Creep. Characterization and Modeling to Control Sintered Ceramic Microstructures and Properties. Ceramic Transactions Series. 2006. p. 49–58. https://doi.org/10.1002/9781118407080.ch6

Figure Captions

Fig. 1. (a) *Hot-pressing situation for case I and* (b) *sinter-forging situation for case II* (*uniaxial stress applied through the piston*).

Fig. 2. *Schematic flow chart for the computation of density evolution*. *H is the powder compact height, R is its radius,* σ_{ij} *is the stress tensor and* ε_{ij} *is the strain tensor*

Fig. 3(a). *Dependence of the relative density on the sintering time for amorphous powder compact for case I (hot-pressing). Lines with squared markers correspond to the temperature T* = 675 ºC; *lines with circular markers to T* = 625 ºC. *The experimental results are for hot-pressing of gel derived sodium borosilicate hot-pressed at* 25 MPa [64].

Fig. 3(b). *Predicted dependence of the relative density on the sintering time for amorphous powder compact for case II (sinter-forging). Lines with squared markers correspond to the temperature T* = 675 ºC*; lines with circular markers to T* = 625 ºC. *The uniaxial stress for sinter-forging is* 10 MPa.

Fig. 4(a). *Dependence of the relative density on the sintering time for alumina powder compact for case I (hot-pressing). Lines with squared markers correspond to the temperature T* = 1450ºC; *lines with circular markers to T* = 1400 ºC. *For both models, the hot-pressing stress is* 10 MPa.

Fig. 4(b). *Predicted dependence of the relative density on the sintering time for alumina powder compact for case II (sinter-forging). Lines with circular markers correspond to the temperature T* = 1400ºC; *lines with squared markers to T* = 1450 ºC. *The sinter-forging stress is* 10 MPa.

Fig. 5(a). *Dependence of the relative density on the sintering time for zirconia powder compact for case II (sinter-forging). Lines with squared markers correspond to the applied stress P* = 8.8 MPa; *lines with circular markers to P* = 17.9 MPa. *For both cases, the temperature is equal to* 1300ºC.

Fig. 5(b). *Dependence of the relative density on the sintering time for zirconia powder compact for case I (hot pressing)*. *Lines with squared markers correspond to the applied stress* P = 8.8 MPa; *lines with circular markers to* P = 17.9 MPa. *For both cases, the temperature is equal to* 1300 ºC.

Fig. 6(a). *Relative density as function of homologous temperature for amorphous powder compact for case I (hot-pressing) at different heating rates with a 10 MPa applied stress*.

Fig. 6(b). *Relative density as function of homologous temperature for polycrystalline ceramics powder for case I (hot-pressing) at different heating rates with a 10 MPa applied stress*.

Table Captions

Table 1. *Four different constitutive behaviors identified in the first column are considered for cases I and II resulting in eight numerical experiments*.

Table 2. *Boundary conditions for the hot-pressing experiments (I) and the sinter-forging experiments (II) problem.*

Table 3. *Skorohod–Olevsky parameters taken from Ref.* [44]. *The radius r is taken from Ref.*[44], *and the surface energy* γ *is an estimation*.

Table 4. *Fitted parameters for the Riedel-Svoboda constitutive law for alumina powder compact densification reported in Ref.* [21] *during hot-pressing.*

Table 5. *Fitted parameters for the Kuhn-Sofronis-McMeeking model to match the alumina powder compact densification reported in Ref.* [21] *during hot-pressing.*

Table 6. *Fitted parameters for the Riedel-Svoboda constitutive law for zirconia powder compact densification reported in Ref.* [26] *during sinter-forging.*

Table 7. *Fitted parameters for the Kuhn-Sofronis-McMeeking model to match the zirconia powder compact densification reported in Ref.* [26] *during sinter-forging.*